PCCP

PAPER

View Article Online
View Journal

Cite this: DOI: 10.1039/c9cp01927h

A charge optimized many-body potential for iron/iron-fluoride systems†

E. Tangarife,[a] A. H. Romero [b] and J. Mejía-López *[a]

Received 6th April 2019,
Accepted 13th August 2019

DOI: 10.1039/c9cp01927h

rsc.li/pccp

A classical interatomic potential for iron/iron-fluoride systems is developed in the framework of the charge optimized many-body (COMB) potential. This interatomic potential takes into consideration the effects of charge transfer and many-body interactions depending on the chemical environment. The potential is fitted to a training set composed of both experimental and *ab initio* results of the cohesive energies of several Fe and FeF_2 crystal phases, the two fluorine molecules F_2 and the F_2^{-1} dissociation energy curve, the Fe and FeF_2 lattice parameters of the ground state crystalline phase, and the elastic constants of the body centered cubic Fe structure. The potential is tested in an *NVT* ensemble for different initial structural configurations as the crystal ground state phases, F_2 molecules, iron clusters, and iron nanospheres. In particular, we model the FeF_2/Fe bilayer and multilayer interfaces, as well as a system of square FeF_2 nanowires immersed in an iron solid. It has been shown that there exists a reordering of the atomic positions for F and Fe atoms at the interface zone; this rearrangement leads to an increase in the charge transfer among the atoms that make the interface and put forward a possible mechanism of the exchange bias origin based on asymmetric electric charge transfer in the different spin channels.

1 Introduction

Iron fluoride (FeF_2) has gained a lot of attention due to the diversity of interesting properties reported to date, such as the spin–phonon interaction,[1] magnon squeezing,[2] temperature dependence of the Raman active phonons,[3] critical behavior of specific heat, thermal diffusivity and conductivity at the Néel temperature,[4] specific capacities and energy densities exceeding those based on $LiCoO_2$ as a result of a type of reversible conversion positive electrode for Li-ion batteries based on FeF_x/C nanocomposites.[5] In particular, the surface of FeF_2 is especially relevant to the understanding of the exchange bias (EB) phenomenon, which has important implications in the sensor industry,[6–8] and has been extensively explored, both theoretically[9] and experimentally.[10]

EB appears when an antiferromagnetic (AF) system is put in contact with a ferromagnetic (FM) material, resulting in shifting of its hysteresis loop along the external field direction.[9,10] Due to the interface nature of this phenomenon, it strongly depends on the AF–FM interface structure and the associated characteristics, such as the crystalline orientation, the interface disorder, interface defects, the presence of twin defects, among other factors. Therefore a complete understanding of these properties requires a good characterization of the structural and the electronic properties of FeF_2, as well as information about the geometric and spin structure at the interface which is difficult to obtain from experimental measurements. Experimental studies[11–14] and *ab initio* calculations[15–19] have shown that bulk FeF_2 is an AF insulator with a strong ionic character. The crystalline structure is a tetragonal rutile with space group $P4_2/mnm$, lattice parameters a = 4.696 Å and c = 3.308 Å with Wyckoff positions 2a (0, 0, 0) for Fe and 4f (x, x, 0), x = 0.3011, for F. FeF_2 has been studied at the atomic level by first-principles calculations but mostly on static configurations though there exist very few molecular dynamics (MD) simulations.[20,21] One of the main reasons why we do not find the characterization of the dynamical properties of Fe/FeF_2 systems is basically because there is not a good classical interatomic potential that reproduces the geometric structure, the structural reconstruction, the magnetic properties and the charging and discharging cycles that involve the multiple valence states of the transition-metal ion, in particular in length scales that involve several hundred or even thousands of atoms.

In addition, there are only very few experimental and theoretical studies on the FeF_2 surface. For example, Yamazaki and Satooka[22] have used molecular beam epitaxy to grow samples of $FeF_2(001)/ZnF_2(001)$ on $Al_2O_3(1010)$ and $FeF_2(110)/ZnF_2(110)$ on MgO(100), with different FeF_2 thicknesses. From their X-ray

[a] Centro de Investigación en Nanotecnología y Materiales Avanzados CIEN-UC, Facultad de Física, Pontificia Universidad Católica de Chile, CEDENNA, Santiago, Chile. E-mail: jmejia@puc.cl
[b] Physics Department, West Virginia University, Morgantown, WV 26506-6315, USA

† Electronic supplementary information (ESI) available. See DOI: 10.1039/c9cp01927h

diffraction measurements, they concluded that the in-plane spacing is identical to the bulk value, while the spacing among different planes falls between both materials' bulk values (3.3091 Å for FeF_2 and 3.1335 Å for ZnF_2) and approaches the ZnF_2 value as the thickness decreases. On the other hand, from a theoretical point of view, Density Functional Theory (DFT) calculations[23,24] were reported for the FeF_2(110) surface by Munoz *et al.*,[20] who showed that there exists surface relaxation on both F- and Fe-terminated surfaces, with the largest displacement occurring F-terminated surfaces. There is a zigzag reconstruction, with half of the Fe atoms displaced 0.2 Å above their nominal bulk position, and the other half displaced about the same amount below that reference position, but the F–Fe bond length remains close to its bulk value (2.04 Å). Similarly, classical MD simulations have been reported by using a variable charge potential developed to simulate how FeF_2 and FeF_3 can be used in energy conversion.[21] They have reported a surface energy decrease when comparing the surface energy to the case where the charge transfer is not taken into account. Although this potential simulates FeF_2 well, it is not transferable to simulate metallic Fe.

To the best of our knowledge, there are no reported theoretical studies of the dynamical properties at the atomic scale of the FeF_2/Fe interface. In this interface, the electrostatic coupling between the FeF_2 and Fe can modify the charge distribution of the different layers close to the interface, as well as providing the conditions to enable atomic Fe migration towards the FeF_2 surface. This effect could be responsible for the uncompensated magnetization necessary to obtain the unidirectional anisotropy responsible for the EB phenomenon.[9] This proposal has not been investigated from first-principles methods, due to the large constraints on the system size and simulated time scales necessary to make appropriate conclusions. On the other hand, classical MD simulations are useful as long as an adequate interaction potential can be developed, which must consider correctly and simultaneously the metallic bond of iron bulk conditions and the ionic bond present in FeF_2. There exist empirical potentials which can be extended to describe a variety of complex chemical bonding environments by using the same theoretical framework, as COMB[25,26] or the reactive force field (ReaxFF).[27] These potentials are flexible enough to allow the investigation of heterogeneous material systems. In particular, COMB has been used to study heterogeneous systems such as oxygen clustering at Zr surfaces and dissociation of O_2 on Zr(0001),[28] deposition of Cu clusters on ZnO surfaces,[29] the tensile properties of Al and Al_2O_3 nanowires,[30] the thermodynamic properties of several interfaces,[31–39] the absorption of oxygen atoms and molecules on the TiN(001) surface[40] and thermal transport in Si–SiO_2 nanostructures.[41]

The purpose of the present work is to present the COMB potential developed for the Fe–F system. The generated potential will be used to investigate the behavior of Fe and FeF_2 magnetic bulks, Fe and FeF_2 surfaces and FeF_2/Fe interfaces in a Large-scale Atomic/Molecular Massively Parallel Simulator[42] (LAMMPS), where the COMB potential is included. All MD simulations are carried out using an *NVT* canonical ensemble where the temperature is controlled through a Nose–Hoover thermostat.[43]

2 Computational methods

2.1 Density functional theory calculations

While a large part of the data used to train our potential came from the experiment, we have also used density functional (DFT) calculations to create some extra data. Here we set the most important properties of the performed DFT calculations.

DFT calculations were performed using the projector-augmented wave (PAW)[44,45] method as implemented in the Vienna *ab initio* simulation package (VASP).[46–49] We use a plane-wave energy cutoff of 520 eV to ensure a high precision in all our calculations. The exchange correlation energy is described within the GGA in the PBE[50,51] prescription. The GGA+U method is used to account for the strong correlation between the electrons in the Fe d shell, on the basis of Dudarev's method.[52] In this method, the on-site Coulomb interaction, U, and the on-site exchange interaction, J^H, are treated together as $U_{eff} = U - J^H$. For our GGA+U calculations we choose U = 6 eV and J^H = 0.95 eV for the Fe atom, which has been previously tested to provide a very good description in FeF_2.[19]

To guarantee that the used data are fairly independent of the chosen exchange correlation functional, we have also calculated some of the properties with the SCAN functional.[53] This functional has been reported to be quite accurate with respect to energies and structural parameters.[54] Our SCAN calculations are very close to those obtained from PBE, and therefore, in the potential training we have only used the PBE results.

2.2 COMB and parameterization formalism

The COMB potential is created on the basis of the interatomic potential propounded by Tersoff[55] with a generalization set out by Yasukawa,[56] which includes the atomic charge as a potential variable. The charge is calculated at every time step using the charge equilibration developed by Streitz and Mintmire,[57] which minimizes the energy function and allows including the effects of the charge transfer among atoms and changes in the local chemical environment.[25,26] In the COMB potential, the total energy (which depends on the charges $\{q\}$ and the atomic positions $\{r\}$) is given by:

$$U^{tot}[\{q\},\{r\}] = U^{es}[\{q\},\{r\}] + U^{short}[\{q\},\{r\}] + U^{vdW}[\{r\}] + U^{angular}[\{r\}] \quad (1)$$

where the electrostatic term U^{es} includes the energy required to change the atomic charge on each atom under isolated conditions, the charge–charge interactions, the core–charge interactions and the energies associated with the polarizability. The short-range energy U^{short} has attractive and repulsive terms dependent on the charge. The charge independent terms include the long-range van der Waals interactions U^{vdW} that

are captured through a Lennard-Jones formula, and an angular correction term $U^{angular}$ that takes into consideration the bond angles not included in the bond-order energy. The complete details of each term in the COMB potential are found elsewhere[26] and they are revisited in Appendix A.

The fitting of the COMB potential is treated like a problem of finding an optimal set of parameters that reproduce a set of calculated or experimental values for a given set of physical properties of the system. The main objective of the parameterization of a potential is to reproduce correctly the structural and mechanical properties of the crystal phase (bulk) in the ground state, and the relative formation of the different accessible phases, keeping at the same time a reliable degree of transferability. Several parameters of the COMB potential are fitted directly from the experimental data, and the remaining parameters are calculated as the minimization of the square difference addition function,[58] through the equation

$$\mathscr{F} = \sum_{i=1}^{N_{obs}} w_i \left(\frac{f_i^{obs} - f_i^{calc}}{f_i^{obs}} \right)^2, \quad (2)$$

where N_{obs} is the number of observables included in the test set, f_i^{obs} are the values of the observables obtained from the experimental data or first principles calculations, f_i^{calc} are the values calculated with the COMB potential, and w_i is the weight factor of each observable. The group of physical properties is composed of the experimental data reported in the literature,[59–62] and some properties not reported experimentally are found from first principles calculations using DFT[23,24] as implemented in the Vienna Ab-initio Simulation package (VASP)[46–49] using the generalized-gradient approximation (GGA)[51] and the Perdew–Burke–Ernzerhof (PBE)[51] exchange–correlation functional. The wavefunctions are expanded in a plane-wave basis set with an energy cutoff of 520 eV. A Monkhorst–Pack k-point mesh[63] is used to describe quantities in the reciprocal space, and projector augmented-wave (PAW) pseudopotentials[44,45] are used for Fe and F. The convergence criteria are set at 10^{-6} eV and 8×10^{-3} eV Å^{-1} for energies and forces, respectively.

The function $\mathscr{F}$ is minimized following two steps. Initially a genetic algorithm[64,65] is used to optimize the parameters in the COMB potential by varying the elements of a population (each element with a different realization of the required parameters) in an ample parameter phase space. As a second step we used a Monte Carlo minimization to the best individual of the population (where the ''best individual'' corresponds to the parameter set with the smaller $\mathscr{F}$ value) in order to refine the global minimum obtained by the genetic algorithm. In the genetic algorithm, each set of parameters is considered like an individual of the population, and the 30% best individuals (in accordance with the fitness function used in the genetic algorithms[65]) are preserved for the next population. New individuals are generated with the following rules:[65] mutation, inversion, arithmetic and geometric mean, and 2-point-crossover.

2.3 Parameterization of atomic and metallic Fe

The cut-off radius for the short-range interactions between Fe–Fe was chosen to capture the first and second neighbors of the lowest energy crystal phase of Fe and first neighbors in the case of FeF_2. The atomic parameters χ_{Fe}, J_{Fe}, K_{Fe} and L_{Fe} that describe the electrostatic self-energy term, U^{self}, shown in eqn (11) are found through the fitting of least squares to the experimental data[66] of the electron affinity and the three first ionization energies of the isolated atom. The lower and upper charge limits $Q_{L_{Fe}}$ and $Q_{U_{Fe}}$ are fixed to $-4e$ and $+4e$ respectively, where e is the electron charge. In the electrostatic energy term for iron bulk structures only the charge-independent terms are needed. The angular function $g(\theta)$ within the bond-order term is fitted so that it represents two minimum energy points in 70° and 110° formed by the first neighbors in the BCC structure. The pair parameters (A_{ii}, B_{ii}, λ_{ii}, and α_{ii}) and the coordination parameters ($c_{ii-0} - c_{ii-3}$) are fitted by minimization of the function $\mathscr{F}$ in eqn (2) considering the cohesion energy data for the ground state BCC, face center cubic (FCC) and simple cubic (SC) stable phases, lattice parameters, and elastic constants. The atomic and pair parameters for Fe are shown in Tables 1 and 2.

2.4 Parameterization of atomic and molecular F

The cut-off radius for the interaction among F atoms is defined according to their mobility in the FeF_2 rutile phase and considering up to fourth neighbors. The atomic parameters χ_F, J_F, K_F and L_F that describe the electrostatic self-energy term, U^{self}, shown in eqn (11) are found using the same process than the Fe isolated atom. The charge independent parameters (A_{ii}, B_{ii}, λ_{ii}, and α_{ii}) are found through the least squares fitting of the bond dissociation energy curve of the F molecule (F_2) calculated by Giner *et al.*[67] using a DFT all electron calculation (full potential DFT). The charge dependent parameters (P_{ii}^{χ}, P_{ii}^{J}, η_i, Z_i, D_{U_i}, D_{L_i}, λ_i, and α_i) are found through the least squares fitting of the bond dissociation energy curve of the ionized F molecule (F_2^{-1}) obtained through DFT calculations. The lower and upper charge limits for Q_{L_F} and Q_{U_F} are set to $-3e$ and $+5e$ respectively. Finally, the many-body bond-order angular parameters (β_{ii}, $b_{ii}^{ang\_0} - b_{ii}^{ang\_6}$) are

Table 1 Atomic and electrostatic parameters of Fe and F for the COMB potential developed in this work

Parameters	Fe	F
χ (eV e^{-1})	5.069430	11.830100
J (eV e^{-2})	3.306150	6.147810
K (eV e^{-3})	−1.036760	−2.619360
L (eV e^{-4})	0.563807	3.503500
η (Å^{-1})	1.489875	0.493250
Z (e)	1.414728	0.000000
P (Å^3)	0.001	0.001
D_U	−1.720391	−2.497540
D_L	2.540010	2.587250
Q_U (e)	4.0	5.0
Q_L (e)	−4.0	−3.0
λ	2.709534	1.629496
α	1.620875	0.639121
m	1.0	1.0
n	1.0	1.0
n_B	10.0	10.0

Table 2 Parameterized parameters and cut-off radii used for Fe–Fe, Fe–F, F–Fe and F–F in the COMB potential developed in this work

Parameters	Fe–Fe	F–F	Fe–F	F–Fe
A (eV)	876.993080	9320.726050	1116.466581	1116.466581
λ (Å^{-1})	2.709534	4.817264	2.929905	2.929905
B (eV)	140.714377	2672.400832	244.603338	244.603338
α (Å^{-1})	1.620875	3.736428	1.946511	1.946511
β (Å^{-1})	2.009266	4.5	1.551968	3.429314
$b^{\mathrm{ang\_0}}$	0.068500	0.795324	0.055085	0.312161
$b^{\mathrm{ang\_1}}$	0.007753	0.910774	0.0	0.154800
$b^{\mathrm{ang\_2}}$	−0.946680	0.198679	−0.037719	0.509100
$b^{\mathrm{ang\_3}}$	0.005296	0.347296	0.009016	0.258240
$b^{\mathrm{ang\_4}}$	4.885325	0.679559	0.442023	−1.111954
$b^{\mathrm{ang\_5}}$	0.013383	0.220316	0.0	−1.008183
$b^{\mathrm{ang\_6}}$	−3.805910	1.480357	−0.461575	0.837549
c_0	0.05	0.0	−0.126193	0.025046
c_1	1.543624	0.0	0.993730	2.5
c_2	−0.15	0.0	0.085114	−0.163767
c_3	−0.683966	0.0	−0.687003	−0.892878
P^{χ} (eV Å^3 e^{-1})	0.0	−1.183010	−0.349429	−0.642628
P^{J} (eV Å^5 e^{-2})	0.0	16.147810	0.846363	−0.860076
A^{χ} (Å^2)	0.0	0.0	0.5	0.5
A^{J} (Å^2)	0.0	0.0	0.5	0.5
ε (eV)	0.0	0.0	0.0	0.0
σ (Å^{-1})	0.0	0.0	0.0	0.0
N^{cross}	1.0	1.0	1.0	1.0
r_c (Å)	3.3	3.7	2.8	2.8
Δ (Å)	0.2	0.2	0.2	0.2
R_{Coulomb} (Å)	11.0	11.0	11.0	11.0

fitted through the minimization of the function $\mathscr{F}$ including the cohesion energy data for the atoms cluster with spherical symmetry. The parameters resulting from the fitting for the interaction among F atoms are shown in Tables 1 and 2.

2.5 Parameterization of iron fluoride

The cut-off radius for the interaction among Fe and F atoms is considered up to first neighbors in the rutile phase of FeF_2. The coordination function P_{ij} in eqn (23) is fitted to have a minimum in the coordination number, Ω_i = 15.0, for fluoride atoms. This function favors the rutile phase, but it does not mean that this is the most stable since P_{ij} only affects the bond-order term ($b_{i\text{-}j}$). The angular correction function in eqn (26) is fitted to have a minimum point at the angles 39.2°, 90° and 140.8° for the Fe–Fe–F atomic triple and, 78.3°, 90° and 101.7° for the F–Fe–F atomic triple, which are the main torsion angles for the rutile phase of FeF_2. The charged chemical environment of FeF_2 in the rutile phase makes it necessary to include the electrostatic parameter (η_i, Z_i, D_{U_i}, D_{L_i}), for the atomic Fe, to be fitted. The remaining parameters plus the parameters aforementioned are fitted by minimization of the function $\mathscr{F}$, including DFT charge reference values, cohesion energies of rutile *Pmnn*, *Pbca*, *Fmmm*, and *Pnma* phases and rutile lattice parameters. The parameters corresponding to the interactions Fe–F and F–Fe are listed in Table 2, and those corresponding to the angular interactions are listed in Table 3.

3 Results and discussion

3.1 Properties of fluorine using the COMB potential

Fig. 1 shows the dissociation energy of the fluorine molecule as a function of the interatomic distance for the neutral (F_2) and ionized (F_2^{-1}) states. Keeping in mind that the charge independent parameters were fit using an all-electron DFT calculation as reported by Giner *et al.*[67] Therefore, it is natural to observe a very good agreement between the COMB potential and the DFT neutral state dissociation energy (F_2). While for the ionized state (F_2^{-1}) the same qualitative behavior is observed between the COMB potential and our DFT calculation. In particular, we found a difference of 0.2 Å in the binding distance between the two calculations. Additionally, the inclusion of the ionized state in the fitting of the COMB potential allows us to reproduce the larger stability of the ionized molecule with respect to the neutral molecule, as well as the nonexistence of a stable distance for the ionized molecule F_2^{-2}, as it is also obtained in our DFT calculations.

Table 3 Angular parameters for the COMB potential developed in this work

Parameters	Fe–Fe–Fe	F–F–F	Fe–Fe–F	F–Fe–F	Fe–F–Fe	Fe–F–F
$K^{\mathrm{lp\_0}}$ (eV)	−0.011048	0.0	0.002300	0.028200	0.028200	0.0
$K^{\mathrm{lp\_1}}$ (eV)	−0.089068	0.0	0.0	0.0	0.0	0.0
$K^{\mathrm{lp\_2}}$ (eV)	−0.020797	0.0	0.034710	−0.037719	0.0	0.0
$K^{\mathrm{lp\_3}}$ (eV)	0.010015	0.0	0.0	0.0	0.0	0.0
$K^{\mathrm{lp\_4}}$ (eV)	0.101801	0.0	−0.118298	0.463981	0.0	0.0
$K^{\mathrm{lp\_5}}$ (eV)	0.045519	0.0	0.0	0.0	0.0	0.0
$K^{\mathrm{lp\_6}}$ (eV)	−0.082077	0.0	0.100795	−0.427058	0.0	0.0

The differences between the properties of the molecule and bulk-type structures are contained in the charge dependent terms of the COMB potential through the field term (U^{field}), which modifies the atomic hardness according to the charged chemical environment and the polar term (U^{polar}). This responds to the changes in the atomic dipolar moment due to potential overlapping in the Coulomb integrals and charge

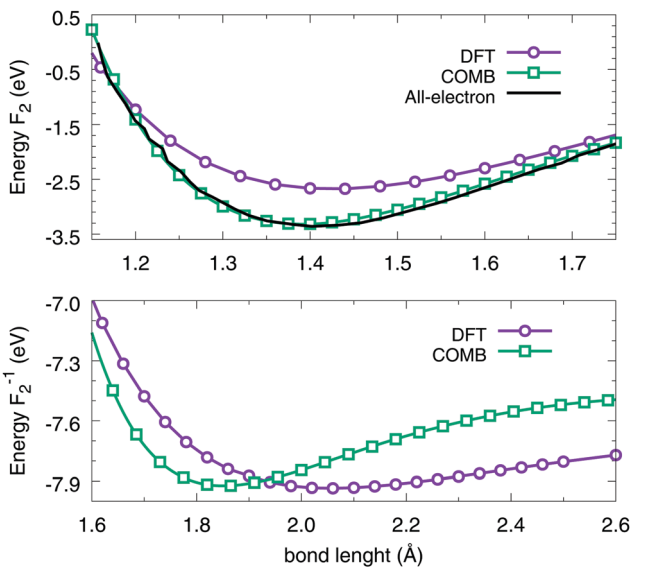

Fig. 1 Bond dissociation energy of F_2 and F_2^{-1} dimers. The black curve corresponds to the data reported by Giner *et al.*[67] from an all electron calculation. The purple circles represent values obtained from DFT calculations and the green squares represent values from the COMB potential.

transfer among atoms with different types of chemical bonding. Thus, the effect of the neutral chemical environment is reproduced in the dimer formation through the bonding term (b_{i-j}) while the other terms are zero. Within this parameter set, the potential reproduces the instability of cluster-type structures, where the cluster cohesivity is due to van der Waals interactions between the dimers without any charge transfer, *i.e.* if *NVT* MD simulations are performed in a cluster formed by N atoms of fluorine, they are separated in gas composed of neutral dimers if the temperature is larger than the small van der Waals cohesive energy.

3.2 Properties of iron using the COMB potential

Table 4 compares the properties of the metallic BCC phase of Fe-bulk predicted by the COMB potential with the experimental[59] data and other reported DFT calculations. The physical construction of the COMB potential provides a good description of the metallic bond at the ground state phase as well as in metastable crystal phases. An important point of the COMB potential fitted here is its ability to reproduce the relative stability and the correct order among the main metallic iron stable phases (BCC, FCC and SC), as shown in Fig. 2. The energy differences between BCC–FCC and BCC–SC are 0.067 eV and 1.5206 eV, respectively, which are in agreement with the differences obtained from DFT calculations. The lattice parameter of the iron ground state calculated using the COMB potential differs by 0.6% compared to the experimental value reported by Rayne and Chandrasekhar.[59] In the same way, the elastic constants are predicted from deviations lower than 16% compared to the experimental values reported by Zotov and Ludwig.[60] The elastic constants obtained in this work are in a better agreement with those obtained from DFT, which have deviations up to 33% (C_{11}). The Fe(110) surface energy,[20] obtained for a slab of 6 nm-thickness with two free surfaces in a box of $20 \times 20 \times 160$ Å^3 with 2170 atoms and with periodic conditions along the [100] and [010] directions, is 124 meV Å^{-2}, in agreement with the DFT calculated value (154 meV Å^{-2}). The last external layers of Fe atoms are dilated 0.31% with respect to the bulk, similar to the DFT value of 0.35%, while the remaining inner atomic layers do not undergo any changes.

Table 4 Properties of iron metal and iron fluoride given by the COMB potential for Fe/FeF_2 developed in this work in comparison with the experimental and DFT calculations

Property	Exp	DFT	Present work
Fe			
a_0 (Å)	2.87 (ref. 59)	2.829	2.830
E_0 (eV per atom)		−5.0037	−5.0037
C_{11} (GPa)	243.1 (ref. 60)	346.52	228.73
C_{12} (GPa)	138.1 (ref. 60)	164.08	146.14
C_{44} (GPa)	121.9 (ref. 60)	136.28	141.36
a_{FCC} (Å)		3.45	3.525
E_{FCC} (eV per atom)		−4.8531	−4.9367
a_{SC} (Å)		2.26	2.275
E_{SC} (eV per atom)		−3.9226	−3.4831
FeF_2			
a_0 (Å)	4.696 (ref. 61)	4.800	4.804
c_0 (Å)	3.308 (ref. 61)	3.324	3.330
E_0 (eV per atom)		−4.0993	−4.0999
C_{11} (GPa)	126.50 (ref. 62)	120.75	131.66
C_{33} (GPa)	184.01 (ref. 62)	164.37	504.41
C_{12} (GPa)	98.72 (ref. 62)	88.90	123.60
C_{13} (GPa)	93.04 (ref. 62)	77.06	79.01
C_{44} (GPa)	36.81 (ref. 62)	33.90	39.08
C_{66} (GPa)	84.37 (ref. 62)	78.84	139.05
q_{Fe} (e)		1.56	1.14
q_F (e)		−0.78	−0.57
E_{Pnmn} (eV per atom)		−4.0946	−4.0948
E_{Pbca} (eV per atom)		−4.0530	−4.0575
E_{Fmmm} (eV per atom)		−3.9985	−3.7459
E_{Pnma} (eV per atom)		−3.8983	−2.8635

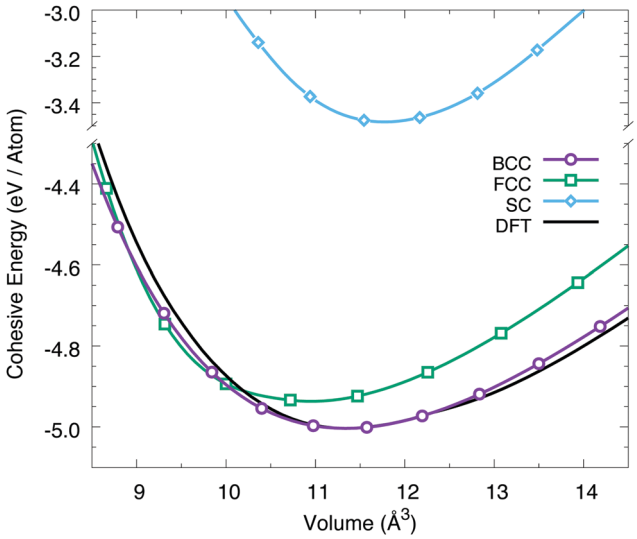

Fig. 2 Cohesive energies as a function of unit volume for Fe phases. The phases shown are BCC represented as the black curve and purple circles, FCC as green squares and SC as cyan rhombuses. The black curve represents the values calculated with DFT and colored symbols represent values from the COMB potential.

We have also tested our COMB potential with the *NVT* simulation of an Fe spherical nanoparticle with 4 nm radius (2861 atoms) using temperatures of 1500 K, 1000 K, 500 K and 10 K. It was found that the nanoparticle at 10 K keeps the BCC phase within it and there is only a small surface reconstruction, which is ordered according to the crystalline directions [110] and [001], as reported experimentally.[68] The charge transfer among atoms is negligible with the most relevant charge values ($\pm 0.04e$) observed at the surface atoms. A binding energy of −4.726 eV, greater than the bulk energy, was obtained. In addition, the Fe–Fe interaction of the COMB potential was tested reproducing stable structures for clusters of Fe atoms between Fe_2 and Fe_{19}. Fig. 3 shows the binding energy as a function of cluster size and it includes a comparison between our results and those available in the literature reported by Q.-M. Ma *et al.*[69] and O. Diéguez *et al.*[70] Our geometries were obtained by using a very simple annealing process as is usually performed when low energy configurations are searched. The binding energy decreases monotonically with an increasing atom-number in the cluster and it can be expected to approach the binding energy of the iron bulk for larger iron clusters. We have obtained the same geometric structures for the ground

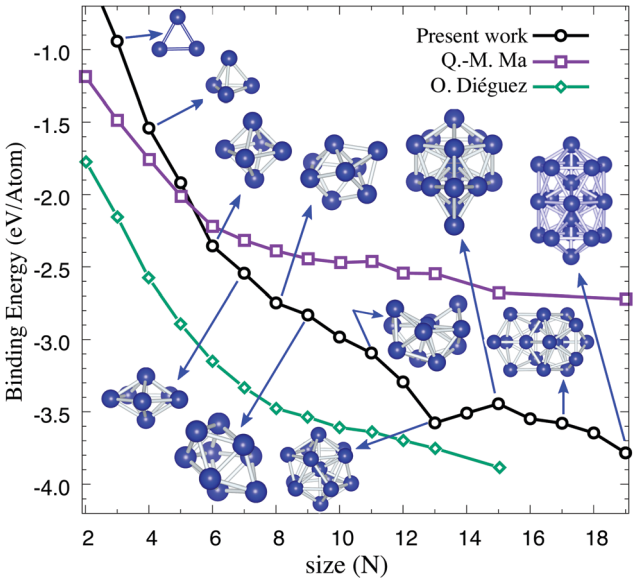

Fig. 3 The binding energies of the global minimum compared with the results by Q.-M. Ma *et al.*[69] and O. Diéguez *et al.*[70] Some of the obtained low energy configurations are included.

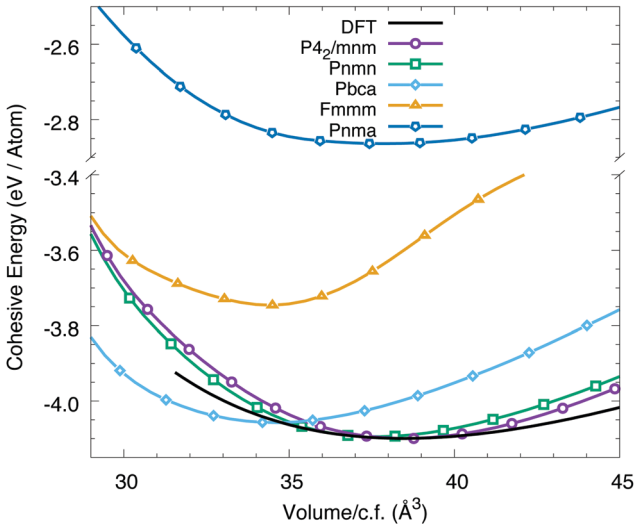

Fig. 4 Cohesive energies as a function of volume for FeF_2 phases. The phases shown are the rutile ($P4_2/mnm$) phase represented as a black curve and purple circles, *Pnmn* as green squares, *Pbca* as cyan rhombuses, *Fmmm* as orange triangles and *Pnma* as blue hexagons. The black curve represents the values calculated with DFT and the colored symbols represent values from the COMB potential.

state as reported by Q.-M. Ma *et al.*,[69] except for $N = 8$ where our ground state seems different from that reported using DFT calculations. This could be contradictory to the DFT results. To address this difference, we have performed an analysis of the different isomers for $N = 8$ obtained by using our COMB potential. Our results indicate that we have recovered all reported isomers as well as the energy classification of each one of them. The only difference is that our ground state is a bit deformed in relation to the one obtained from DFT, as the angular contribution is more important. We cannot relax this term more, as it is necessary to stabilize correctly the different phases of bulk Fe.

3.3 Properties of iron fluoride using the COMB potential

The structural parameters of the FeF_2 rutile phase ($P4_2/mnm$ the ground state symmetry) calculated with the COMB potential are compared to the experimental[61] data and DFT[19] calculations in Table 4. The calculated COMB potential lattice parameters, a_0 and c_0, are found with a difference of 0.2%. In addition, the atomic charge found with the COMB potential differs by 27.1% regarding the DFT atomic charge Bader analysis. The decrease in the calculated charge value in relation to the stoichiometric reference value [+2, −1] is due to a mix of the ionic and covalent bonds, which depends strongly on the parameters in the COMB potential. The elastic constants derived from our potential are in good agreement with the experimental values.[62] The COMB calculated cohesive energy as a function of volume for several stable phases of FeF_2 is shown in Fig. 4. A good agreement for the structural parameters of the rutile phase with respect to DFT calculations is found, as well as the right energetic order for different metastable phases. Moreover, it is important to emphasize that this COMB potential predicts the correct geometric structure and the stability of the FeF_3 ground state (a trigonal structure with $R\bar{3}c$ ground state symmetry), with lattice parameters of $a = 4.87$ Å and $c = 13.41$ Å, in agreement with previous work[21] and our DFT calculations.

Fig. 5 shows the radial distribution function (RDF) and the angular distribution function (ADF) for the rutile phase with two different temperature values, and those obtained from DFT are also shown for comparison. RDF and ADF are obtained

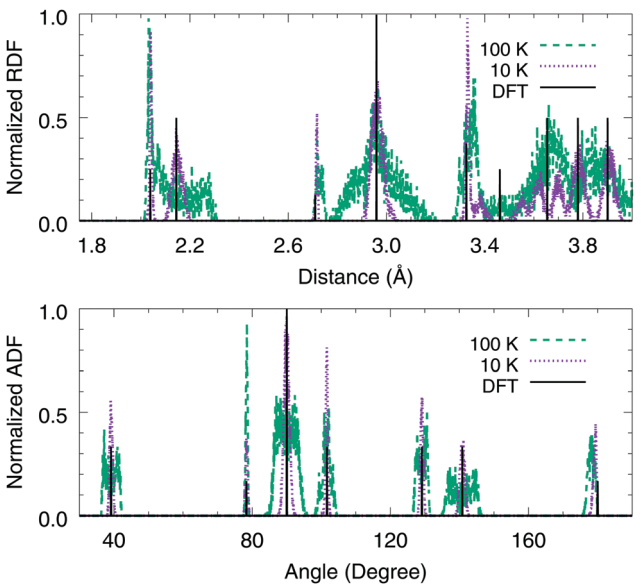

Fig. 5 Radial and angular distribution functions of FeF_2. The solid line represents the peak positions and the angles that are derived from the DFT calculations in the rutile structure. The pointed (green) and dashed (purple) discontinuous lines represent the MD average at 10 K and 100 K.

from the MD simulations with a cell of 33 × 27 × 27 Å^3 with 1920 atoms, averaged during a simulation time of 50 ps. There exists a good overall agreement in the positions of the peaks in comparison to the DFT results, where broadened peaks come from the highest atom mobility related to temperature effects. In particular, it is observed that the COMB potential is able to differentiate the first two peaks in spite of being very close to each other. The F–F peaks are more prone to change with temperature because fluorine atoms have the highest mobility around their equilibrium positions. The peak located at ≈3.46 Å is displaced to the right and to the left taking values of ≈3.35 Å and ≈3.6 Å because of the thermal movement. The Fe–F peak located in ≈3.65 Å splits into two peaks, due to the asymmetry in the elastic constants in the principal directions C_{11}, C_{22} and C_{33}, and the anisotropy in the Debye Waller coefficient.[71] The angular distribution function shows a good agreement with the Fe–Fe–F, F–Fe–F and Fe–F–Fe angles obtained from DFT calculations. The peaks at 38°, 90° and 142° are related to the angles between Fe–Fe–F; 78°, 90°, 102° and 180° are related to the angles between F–Fe–F, and 102° and 128° are related to the angles between Fe–F–Fe.

The averaged MD atomic charges obtained for the rutile FeF_2 phase (at zero pressure and 10 K) are shown in Fig. 6. The average equilibrated charge was modeled with a Gaussian distribution function. We found that, at 10 K, there exist charge differences of up to 7% for all different considered phases with respect to the rutile phase. This is comparable to changes of 1% obtained by the atomic charge Bader analysis calculated from DFT calculations (at 0 K). On the other hand, the room temperature effect over the average equilibrated charge in the rutile phase only affects the standard deviation of the Gaussian distribution function; this increases the average equilibrated by 0.3%. In this way, the charges are very stable regarding the geometric structure and the temperature.

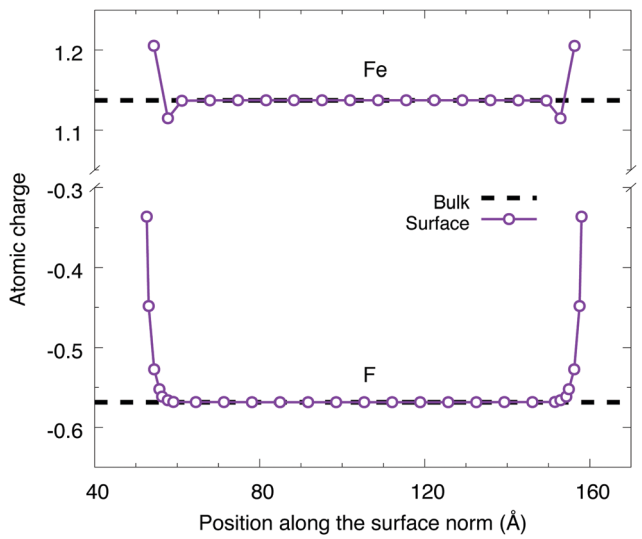

Fig. 6 Charge distribution of FeF_2 in the case of the rutile structure (black dashed line) and along the surface norm (110) surface with fluorine terminations (purple circles).

3.4 Behavior of the FeF_2 surface

The initial FeF_2(110) surface structure is generated from the relaxed bulk structure, where the z-axis points out in the [110] direction, including an empty space of 50 Å to avoid interaction with its periodic images. In this form, a slab of 93 Å with two free surfaces is simulated in a box of 20 × 20 × 193 Å^3 with 2952 atoms. Fig. 7 shows a surface snapshot of FeF_2, where the slab layers are alternated between Fe–F and F layers, with terminations with fluorine layers for both free surfaces. We chose this type of surface orientation particularly because this orientation exhibits a remarkably large EB field and it is more stable energetically than the surface with Fe termination.[20] The surface is made of layers I to VII, as the remaining inner atomic layers do not undergo any change in this slab geometry. The calculated interlayer relaxations are as follows: $\Delta d_{\text{I–II}} = -31.7\%$, $\Delta d_{\text{II–III}} = -11.6\%$, $\Delta d_{\text{III–IV}} = 5.2\%$, $\Delta d_{\text{IV–V}} = -11.0\%$, $\Delta d_{\text{V–VI}} = 0.4\%$, and $\Delta d_{\text{VI–VII}} = 3.4\%$. The compression and dilation between the different layers generate new peaks in the radial function distribution (see Fig. 8) in comparison with the bulk radial function. In particular, the peaks at ≈2.6 Å and ≈2.8 Å correspond to bonds between fluorine atoms belonging to the II and IV layers, and to the I and III layers but now at a distance of ≈2.8 Å. The peak at 1.97 Å corresponds to the bond between the fluorine atoms from layers I and V and the iron atoms in layer III. The approach of the fluorine atom layers that surround the iron and the surface fluorine layer reconstruction (compression of layers II and IV with respect to layer III) generates two new angles in the F–Fe–F angular distribution of 75° and 110° and two new angles between Fe–Fe–F triples at 35° and 144°, and a new angle for the triple Fe–F–Fe at 110°. There is also peak widening in peaks at 38°, 90°, 100°, 140° and 180°.

The FeF_2(110) surface charge distribution with the fluorine termination is shown in Fig. 6. The superficial atoms show an increase in the average charge of 6% with respect to bulk. This result agrees with DFT calculations, which show an increase in the charge of the superficial atoms of 12%. The surface reconstruction is very small and the surface atom positions remain close to those in the bulk. The COMB surface energy is overestimated with respect to the DFT value, which is 179 meV Å^{-2}

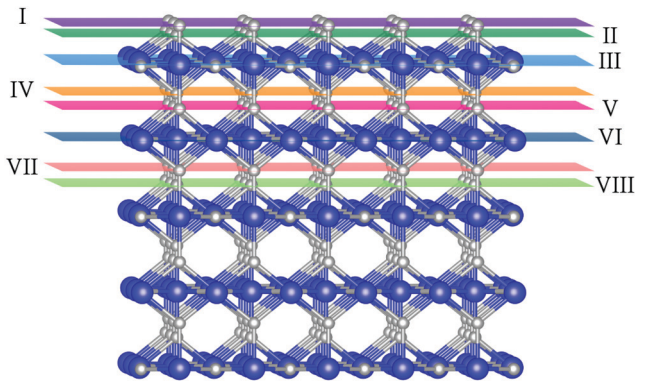

Fig. 7 Snapshot of the surface structure of FeF_2 obtained by MD simulations. We label in Roman numerals the layers that compose the surface.

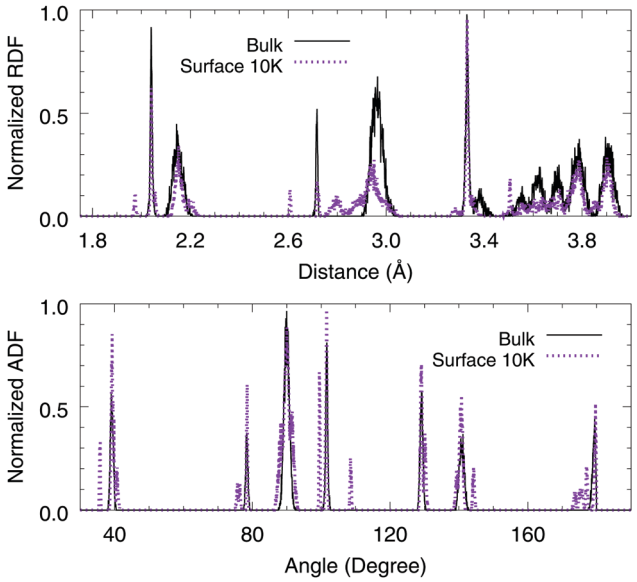

Fig. 8 Radial and angular distribution functions of the surface of FeF_2. The black solid line represents the peak positions and angles that are derived from the MD average for the FeF_2 rutile phase at 10 K calculations and the purple dashed line represents the MD average for the FeF_2(110) surface at 10 K.

for the COMB potential and 57.1 meV $Å^{-2}$ for DFT. This overestimation is due to the angular term in the COMB potential, which affects the short-range attraction and repulsion of the surface atoms, but it is necessary in the FeF_2 in order to obtain a stable surface structure.

3.5 FeF_2/Fe interface

From a magnetism point of view, FeF_2 is AF while Fe is FM. When they are in contact, EB (displacement of the hysteresis loop) is obtained, which is mainly an interfacial phenomenon.[9] The atomic structure of the FeF_2/Fe interface is not yet well understood. In this section we attempt to give an overview of the interface atomic structure obtained by means of *NVT* MD simulations using the parameterized COMB potential. The structures studied consist of a 6 nm-thick slab of Fe interfaced with a 9 nm-thick slab of FeF_2. Periodic boundary conditions are applied in three and two dimensions; in other words, we simulate both an FeF_2/Fe heterostructure and an FeF_2/Fe bilayer. In order to obtain a thermodynamically stable state of the interface, we performed temperature annealing with different initial temperatures: (i) 1000 K, lower than the melting point of FeF_2 and Fe bulks. (ii) 1500 K, higher than the melting point of the FeF_2 bulk and lower than the melting point of the Fe bulk. (iii) 2000 K, higher than the melting point of FeF_2 and Fe bulks. Next, we started to cool the system at a rate of 100 K every 10 ps until reaching 10 K where we allowed the system to equilibrate for a time of 60 ps. Each of these procedures leads to similar results: there is no geometric reconstruction at the interface zone, but there is relaxation of the interface atoms of both materials, generating bonds among the F in FeF_2 and Fe in FM in order to compensate their coordination number.

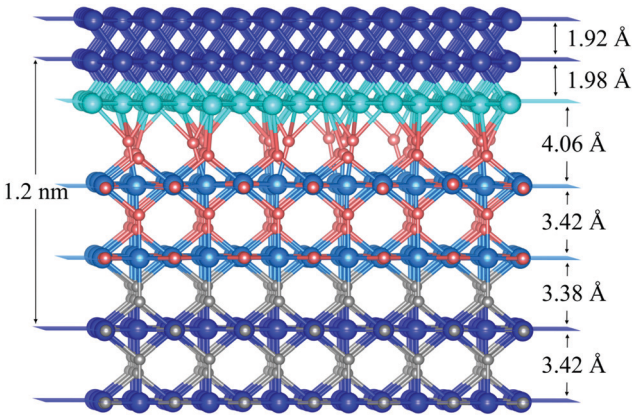

Fig. 9 Snapshot of the interface FeF_2/Fe heterostructure obtained from *NVT* MD simulations. The blue and gray spheres represent Fe and F atoms in their respective bulk counterpart, the turquoise spheres represent Fe atoms forming the interface and coming from the Fe slab and the sky blue and red spheres represent Fe and F atoms forming the interface and, coming from the FeF_2 slab, respectively. Here we have defined as interface atoms those which have effective charges different from the reference COMB potential values obtained in the bulk configuration (see Fig. 11).

This implies charge transfer with a different distribution from that in the bulk, which can define a 1.2 nm-long interface zone. Fig. 9 shows the final structure found (all considered temperatures provided a similar picture). The atoms forming the interface were drawn with different colors as discussed in the figure caption.

Fig. 10 shows the comparison between RDFs for the Fe atoms layers in the Fe and FeF_2 bulk, in the Fe and FeF_2

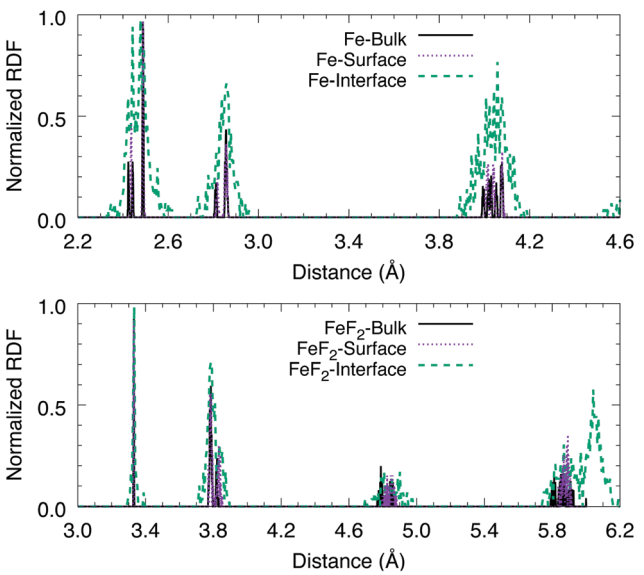

Fig. 10 Radial distribution functions of the Fe atoms at the bulk, surface and interface in the FeF_2/Fe heterostructure at 10 K, after temperature annealing. The black solid line represents the peak positions of the FeF_2 and Fe bulk, the purple dotted line represents the peak positions of FeF_2 and Fe surfaces, and the green dashed line represents the peak positions of the FeF_2 and Fe interface.

surfaces, and in the interface FeF_2/Fe. The Fe RDFs per layer in the Fe-bulk and on the Fe-surface do not show changes in the positions of the characteristic peaks with respect to the bulk BCC structure. This is due to the low Fe mobility as compared to F. As shown in Fig. 10 there are new peaks present in the RDF from the layers close to the interface due to new F–Fe and F–F bonds. On the other hand, in the Fe RDF from the FeF_2/Fe interface layers, some of the peaks broaden due to the generation of new bonds at the interface zone with values close to the bulk. As some of the Fe–F and Fe–Fe distances increase, the Fe atom mobility is larger, as it is weakly bonded as compared to the bulk. The obtained Fe roughness at the interface layers is small, 0.15 Å for the Fe layer and 0.07 Å for the FeF_2 layer. However, it is a noticeable increase in comparison to the Fe roughness in the bulk (0.03 Å for Fe and 0.02 Å for FeF_2).

The interface energy can be calculated as $E_I = (E_{Fe\text{-}slab} + E_{FeF_2\text{-}slab} - E_{FeF_2/Fe})/A$, where each energy is evaluated in the relaxed structure and A is the surface area. It was found that the interface energy obtained by the annealing temperature procedure is 0.768 eV $Å^{-2}$. The distribution of the charge average at the interface for the most stable FeF_2/Fe heterostructure and at a temperature of 10 K is shown in Fig. 11. The new Fe–F bonds at the interface produce an increase in the charge transfer between Fe and F atoms. The absolute value of the atomic F charge average increases since they share bonds with more Fe atoms (the coordination number increases) compared to the FeF_2 bulk. Similarly, the charge average of the Fe atoms decreases with respect to the FeF_2 bulk, while the charge of the surface Fe atoms increases due to the bonding with fluoride atoms. The interface Fe atoms have charge values varying from $-0.2e$ up to $0.5e$.

The second structure studied consists of a FeF_2 nanowire with a transverse section of 2 nm × 2 nm embedded in a BCC Fe crystal. Periodic boundary conditions are applied in three dimensions, and the last environment is big enough to avoid the interactions among nanowires; in other words, we simulated an array of FeF_2 nanowires separated at a distance of 3 nm. With the objective of finding the thermodynamically stable state of the interface, we follow the same annealing procedure aforementioned with an initial temperature of 1500 K. The atoms at the interface zone presented a reordering in their atomic positions. This reordering generated structural changes regarding the initial positions of the structure. Fig. 12 shows a snapshot of the structure found after the annealing procedure. The atoms forming the interface were drawn following the same color convention discussed before.

Fig. 13 shows the RDF and ADF for the FeF_2/Fe interface. A short-range interaction with three mean values around 2.1 Å, 2.45 Å and 2.9 Å is observed. The first and second values correspond to the F–Fe and Fe–Fe atomic distances, which are favored by new bonding at the interface zone. The third value corresponds to the combination of Fe–Fe and F–Fe atomic distances. In the same way, ADF shows a generalized broadening in all RDF and ADF peaks, allowing the presence of new angles favored by the new bonds in the interface zone. The distribution of the charge average for the stable FeF_2/Fe nanowire at a temperature of 10 K is shown in Fig. 14. The atoms in the interface zone present a reconstruction of their atomic positions due to new Fe–F and Fe–Fe bonds generated during the annealing. These new bonds increase the charge transfer among F and Fe atoms. The Fe charge average decreases at the interface in the FeF_2 system

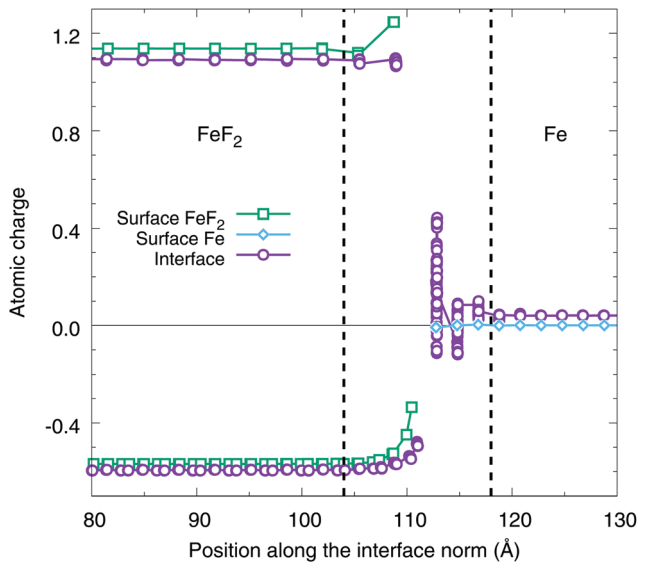

Fig. 11 Charge distribution along the [110] direction of the interface FeF_2/Fe (purple circles), the FeF_2 surface (green squares) and the Fe surface (cyan diamonds).

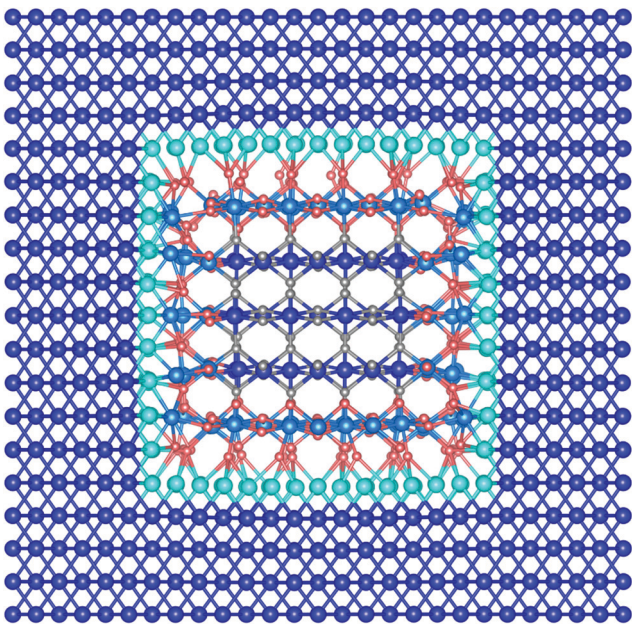

Fig. 12 Snapshot of the interface FeF_2/Fe nanowire obtained by MD simulations. The blue and gray spheres represent Fe and F atoms in their respective bulk counterpart, the turquoise sphere represents Fe atoms coming from the Fe environment and the sky blue and red spheres represent Fe and F atoms coming from FeF_2 nanowires, respectively.

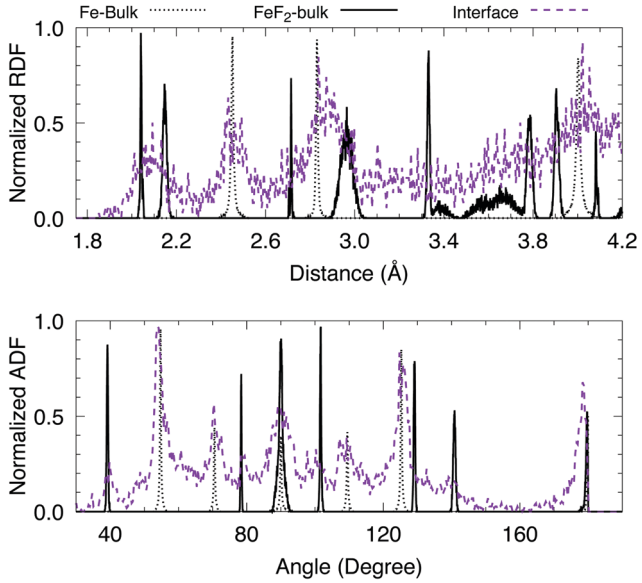

Fig. 13 Radial and angular distribution functions of the interface of the FeF_2/Fe nanowire. The black solid and dotted lines represent the peak positions and angles of the bulk of FeF_2 and Fe, respectively, and the purple dashed line represents the interface region at 10 K, after temperature annealing.

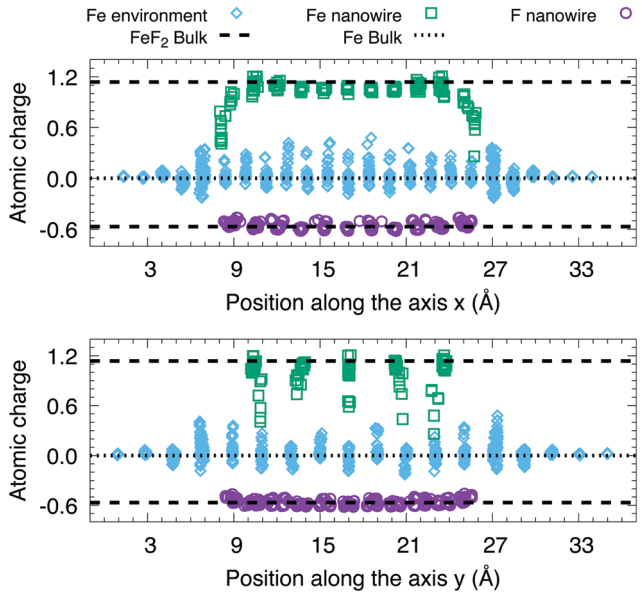

Fig. 14 Charge distribution of the FeF_2 rutile bulk structure (black dashed line), the Fe BCC bulk structure (black dotted line), and along [100] and [010] directions of the interface FeF_2/Fe. Fe in the Fe environment (cyan diamonds), Fe in the FeF_2 nanowire (green squares) and F in the FeF_2 nanowire (purple circles).

with respect to the FeF_2 bulk, while the interface Fe atoms belonging to the Fe crystal phase show a charge increase, as there is an increase in Fe–Fe and Fe–F neighbors. At the same time, the appearance of new bonds due to the atomic reconstruction at the interface zone promotes an increase in the roughness of around 0.33 Å.

The observed atomic structural relaxation and the change in the charge transfer at the interface can be a possible mechanism to the origin of the unidirectional anisotropy necessary to explain the exchange-bias phenomenon. Due to the generation of new bonds in the interface zone, the atoms that make part of the interface present a more important charge transfer than the bulk atoms, as shown in Fig. 11. The electric charge transfer is associated mainly with the Coulomb term U^{Coul}, as seen in eqn (6), through the charge density. Because in a magnetic system the charge density, for both spin channels, is different, the charge transfer at the interface can be different for each spin channel. Therefore, non-compensated magnetic moments at the interface would be created, which through exchange coupling with the ferromagnetic layers of the Fe film would originate an effective unidirectional anisotropy. These unbalanced magnetic moments would freeze during the hysteresis loops because at low temperatures the interface atoms do not show an appreciable change in their positions and therefore, there is no extra charge transfer. This is equivalent to a frozen uniaxial anisotropy as the one proposed by Kiwi *et al.*,[72,73] which explains not only the magnitude of the exchange-bias phenomenon in compensated surfaces, but also the positive and negative dependence of the exchange-bias phenomenon[74] and the asymmetries in the magnetization curves.[75]

4 Conclusions

We have obtained parameterization of the COMB potential for iron and iron fluoride, which takes into consideration the effects of atomic charge transfer and many-body interactions depending on the chemical environment. Using classical *NVT* MD simulations, as implemented in the LAMMPS code, we verified that this potential reproduces the physical properties of the metallic iron in the BCC phase, the dissociation energy curve for F_2 and F_2^{-1} molecules and the rutile phase of FeF_2. The new group of parameters is found to satisfy model atomic clusters, magnetic bulks, surfaces and interfaces between the different materials, demonstrating the capacity of the potential to capture different types of atomic local chemical environment. The potential describes successfully the ground state and the properties of FeF_3, which was not considered initially in the training set. This potential has been used to study the properties of the FeF_2 surface and FeF_2/Fe heterostructures in order to obtain a deeper understanding of the atomic structure of these systems. The *NVT* MD simulation of the interface of FeF_2/Fe shows a reordering of the atomic positions of the F and Fe atoms in the interface zone generated by the temperature annealing procedure. For the interface zone charge transfer is an important property for the formation of ionic bonds between Fe and FeF_2, and all this is activated by the process of cooling from high to low temperatures. This spin dependence electric charge transfer could be a mechanism that explains the exchange bias origin in ferromagnetic/antiferromagnetic systems. The COMB parameterization for Fe and F, which can be used directly in the LAMMPS code, can be downloaded from ref. 76 and some movies

showing the dynamics obtained for the considered systems can be downloaded from the same directory.

Conflicts of interest

There are no conflicts of interest to declare.

Appendix

A Details of the COMB potential

The electrostatic energy U^{es} for a charged atom system shown in eqn (3) includes: the Coulomb interaction energy (U^{Coul}) between charge–charge and charge–core type charged ions, the self-energy for charged atoms (U^{self}), the effect field energy (U^{field}) and the polarization energy (U^{polar}).

$$U^{es} = U^{Coul} + U^{polar} + U^{self} + U^{field}. \quad (3)$$

The large range electrostatic interaction between a pair of charged ions is described by Coulomb's law. When the distance between the ions tends to be zero, the Coulomb interaction tends to infinity. This behavior is known as the Coulomb Catastrophe and is considered by the COMB potential through a density charge function expressed as the spherical distribution function $\rho_i(\mathbf{r},q_i)$ proposed by Streitz and Mintmire,[57]

$$\rho_i(\mathbf{r},q_i) = Z_i\delta(|\mathbf{r} - \mathbf{r}_i|) + (q_i + Z_i)f_i(|\mathbf{r} - \mathbf{r}_i|), \quad (4)$$

$$f_i(|\mathbf{r} - \mathbf{r}_i|) = \frac{\eta_i^3}{\pi}\exp[-2\eta_i|\mathbf{r} - \mathbf{r}_i|], \quad (5)$$

where $\delta(|\mathbf{r} - \mathbf{r}_i|)$ is the Dirac delta function for the effective point charge of the core, $f_i(|\mathbf{r} - \mathbf{r}_i|)$ is a radial distribution function that models the decrease of the valence electronic density like an orbital 1s-Slater[77] and the parameter η_i is the orbital exponent that controls the effective distance of the radial distribution function. The Coulomb interaction energy is calculated as the two center double integral of the product of the total charge density for a pair of atoms i and j.

$$U^{Coul} = \sum_i \sum_{i>j} U_{ij}^{Coul},$$
$$U_{ij}^{Coul} = \int d^3\mathbf{r}_1 \int d^3\mathbf{r}_2 \frac{\rho_i(\mathbf{r}_1, q_i)\rho_j(\mathbf{r}_2, q_j)}{|\mathbf{r}_1 - \mathbf{r}_2|}. \quad (6)$$

The analytic solution of the double integral was found using the procedure proposed by Streitz and Mintmire,[57] where the solution can be written in two principal terms:[78] one term $1/r_{ij}$ that is conditionally convergent and that we added directly using the technique described by Wolf,[79] and the other term multiplied by an exponential function that decreases quickly with the distance.

The atomic polarization is considered as distortions and fluctuations in the charge density around the atom in response to the electric field generated by the variations in the overlapping of the valence charge density;[80,81] that is, the charge exchange among atoms. The dipolar moments induced at each atomic point due to the total electric field are given by:

$$\mu_i = P_i[E_i^q + E_i^D], \quad (7)$$

where P_i is the atomic polarizability of the atom i which is an adjustable parameter of the potential, E_i^q is the electric field generated by the charged atoms adjacent to i, and E_i^D is the dipolar electric field generated by the dipolar moments adjacent to i,

$$E_i^q = \sum_{j\neq i} q_j \frac{\partial J_{ij}^{qq}}{\partial r_{ij}}\frac{r_{ij}}{r_{ij}}, \quad (8)$$

$$E_i^D = -\sum_{j\neq i}\left[\frac{\mu_j}{{r_{ij}}^3} - 3\frac{(\mu_j \cdot r_{ij})\, r_{ij}}{{r_{ij}}^5}\right]. \quad (9)$$

The polarization energy (U^{polar}) is formed by the dipole self-energy, the dipole–electric field and the dipole–dipolar field interaction energies considered as the negative of the dipolar moment by the electric field.

$$U^{polar} = \sum_i \frac{1}{2}\left[\frac{{\mu_i}^2}{P_i} - \mu_i \cdot \left(E_i^q + E_i^D\right)\right], \quad (10)$$

The dipoles induced are calculated in a self-consistent way at every time step in the same way as the charge equilibration and undergo the same instability for very short distances than the charge variables, and as a consequence the dipolar moment is multiplied by a damping function.

The self-energy (U^{self}) is the energy that is required to charge an atom in an isolated chemical environment and it is expressed by the expansion in the Taylor's series regarding the charge (eqn (11)), where χ, J, K and L are the adjustable parameters of the COMB potential. The final term is an energy barrier to penalize charge values out of the allowed range defined by Q_L and Q_U that represent the lower and upper charges for each atomic species.

$$U^{self} = \sum_i \left[\chi_i q_i + J_i {q_i}^2 + K_i {q_i}^3 + L_i {q_i}^4 + 100\left(q_i - q_i^{lim}\right){q_i}^4\right]. \quad (11)$$

The field energy U^{field} represents the correction to electronegativity and the atomic hardness due to the chemical bonds that each atom experiments as a result of the local chemical environment.[82] P_{ij}^{χ}, P_{ij}^{J}, A_{ij}^{χ} and A_{ij}^{J} are the adjustable parameters of the COMB potential,

$$U^{field} = \sum_i \sum_{j>i}\left(\frac{P_{ij}^{\chi} q_j}{{r_{ij}}^3 + \left(\frac{A_{ij}^{\chi}}{r_{ij}}\right)^3} + \frac{P_{ij}^{J} {q_j}^2}{{r_{ij}}^5 + \left(\frac{A_{ij}^{J}}{r_{ij}}\right)^5}\right). \quad (12)$$

The bond-order type short-range energy (U^{short}) is based on the Tersoff potential[55] with a repulsive term (U_{ij}^{R}), and an attractive term (U_{ij}^{A}) joined by one charge independent bond term (b_{i-j}). Originally the short-range energy only depends on the interatomic distance (r_{ij}). Nevertheless, in the COMB

potential, the short-range energy depends on the interatomic distance (r_{ij}) and the atomic charge (q_i,q_j),[56]

$$U^{\text{short}} = \sum_i \sum_{j>i} F_c(r_{ij}) \left[U_{ij}^{R} - b_{i-j} U_{ij}^{A} \right], \tag{13}$$

$$\begin{aligned} U_{ij}^{R} &= A_{ij} \exp\left[-\lambda_{ij} r_{ij} + \lambda_{ij}^{*}\right], \\ \lambda_{ij}^{*} &= \frac{1}{2}\left[\lambda_i D_i(q_i) + \lambda_j D_j(q_j)\right], \end{aligned} \tag{14}$$

$$\begin{aligned} U_{ij}^{A} &= B_{ij} B_{ij}^{*} \exp\left[-\alpha_{ij} r_{ij} + \alpha_{ij}^{*}\right], \\ \alpha_{ij}^{*} &= \frac{1}{2}\left[\alpha_i D_i(q_i) + \alpha_j D_j(q_j)\right], \end{aligned} \tag{15}$$

The dependence with the charge is considered through λ_{ij}* and α_{ij}* which modify the exponential coefficient of the attraction and repulsion energies, reflecting changes in the effective distance of the interaction among charged atoms. D_U and D_L are the adjustable parameters of the COMB potential that reflect the differences in the atomic radius between the neutral and charged atoms,

$$D_i(q_i) = D_{U_i} + \left| \frac{(Q_{U_i} - q_i)(D_{L_i} - D_{U_i})^{\frac{1}{n_{D_i}}}}{Q_{U_i} - Q_{L_i}} \right|^{n_{D_i}} \tag{16}$$

$$n_{D_i} = \frac{\ln(D_{U_i}) - \ln(D_{U_i} - D_{L_i})}{\ln(Q_{U_i}) - \ln(Q_{U_i} - Q_{L_i})}, \tag{17}$$

and additionally, the charge dependence is considered as the attractive term through the function $B_{ij}^{*} = \sqrt{B_i^{*}(q_i) B_j^{*}(q_j)}$, which is equal to the unit for charge within the allowed range and zero elsewhere. Q_0 and ΔQ are the semi-addition and the semi-subtraction between Q_U and Q_L, which together with A, B, λ, α, D_U, D_L and n_B are the adjustable parameters of the COMB potential,

$$B_i^{*}(q_i) = \left[a_{B_i} - \left| \frac{(q_i - Q_{0_i}) |a_{B_i}|^{\frac{1}{n_{B_i}}}}{\Delta Q_i} \right|^{n_{B_i}} \right], \tag{18}$$

$$a_{B_i} = \left(1 - \left| \frac{Q_{0_i}}{\Delta Q_i} \right|^{n_{B_i}} \right)^{-1}. \tag{19}$$

The b_{i-j} in eqn (13) is the semi-addition of bond-order parameters[83] b_{ij} and b_{ji}, and both modify the attraction energy regarding the local chemical environment, including the effect of the neighbor atoms (k-atom) to the atom i in the bond ij and to the atom j in the bond ji,

$$b_{ij} = \left\{ 1 + \left[\sum_{k \neq i,j} \zeta_{ijk} g_{ij}(\theta_{jik}) + P_{ij} \right]^{n_i} \right\}^{-1/2n_i} \tag{20}$$

$$\zeta_{ijk} = F_c(r_{ik}) N_{ik}^{\text{cross}} \exp\left[\beta_{ij}^{m_i} \left(r_{ij} - r_{ik} \right)^{m_i} \right], \tag{21}$$

$$g_{ij}(\theta_{jik}) = \sum_{n=0}^{6} b_{ij}^{\text{ang\_}n} \cos^n(\theta_{jik}), \tag{22}$$

$$P_{ij} = c_0 \Omega_i + c_1 \exp[c_2 \Omega_i] + c_3, \tag{23}$$

where ζ_{ijk} is a screening function on the bonds, g_{ij} and P_{ij} are the angular and coordination functions, respectively, that allow characterization of the flexibility and the anisotropy of the local chemical environment, Ω_i is the number of neighbors (not including j) around the atom i and θ_{jik} is the angle formed by the vectors r_{ij} and r_{ik} with a vertex in the i atom. β, n, m, $b^{\text{ang\_0}} - b^{\text{ang\_6}}$, $c_0 - c_3$ and N^{cross} are adjustable parameters of the COMB potential. The function $F_c(r)$ is a cut-off function Tersoff type[55] which ends smoothly the region of interaction between the cut-off radius $R = r_c - \Delta$ and $S = r_c + \Delta$, with r_c and Δ being the adjustable parameters of the COMB potential,

$$F_c(r_{ij}) = \begin{cases} 1 & r_{ij} \leq R_{ij}, \\ \frac{1}{2}\left[1 + \cos\left(\frac{\pi(r_{ij} - R_{ij})}{S_{ij} - R_{ij}} \right) \right] & R_{ij} < r_{ij} \leq S_{ij}, \\ 0 & r_{ij} > S_{ij}. \end{cases} \tag{24}$$

The long-range interaction of van der Waals is considered by Lennard-Jones' classic formula, where ε_{ij} and σ_{ij} are the intensity and the distance of equilibrium for the van der Waals interaction and are the adjustable parameters of the COMB potential,

$$U^{\text{vdW}} = \sum_i \sum_{j>i} 4\varepsilon_{ij} \left[\left(\frac{\sigma_{ij}}{r_{ij}} \right)^{12} - \left(\frac{\sigma_{ij}}{r_{ij}} \right)^{6} \right]. \tag{25}$$

The charge independent angular interaction is included to describe the direction of the bonds present in the local environment,[84] where $K_{jik}^{\text{lp\_}0} - K_{jik}^{\text{lp\_}6}$ are the adjustable parameters of the COMB potential,

$$U^{\text{angular}} = \frac{1}{2} \sum_i \sum_{j \neq i} \sum_{k \neq i,j} \left\{ F_c(r_{ij}) F_c(r_{ik}) \times \sum_{n=0}^{6} K_{jik}^{\text{lp\_}n} \cos^n(\theta_{jik}) \right\}. \tag{26}$$

Acknowledgements

We acknowledge support from the Fondecyt grant 1130672 and Financiamiento basal para centros científicos y tecnológicos de excelencia FB 0807. E. T. acknowledges support received from the Conicyt Fellowship CONICYT-PCHA/Doctorado Nacional/2015-04270947. His work used the XSEDE which is supported by the National Science Foundation grant number ACI-1053575. The authors also acknowledge the support from the Texas Advances Computer Center (with the Stampede2 and Bridges supercomputers), and AHR was supported by the DMREF-NSF 1434897, NSF OAC-1740111 and DOE DE-SC0016176 projects.

References

1 D. J. Lockwood and M. G. Cottam, *J. Appl. Phys.*, 1988, **64**, 5876–5878.
2 J. Zhao, A. V. Bragas, R. Merlin and D. J. Lockwood, *Phys. Rev. B: Condens. Matter Mater. Phys.*, 2006, **73**, 184434.
3 D. J. Lockwood, R. S. Katiyar and V. C. Y. So, *Phys. Rev. B: Condens. Matter Mater. Phys.*, 1983, **28**, 1983.
4 M. Marinelli, F. Mercuri and D. P. Belanger, *Phys. Rev. B: Condens. Matter Mater. Phys.*, 1995, **51**, 8897–8903.
5 F. Cosandey, J. F. Al-Sharab, F. Badway, G. G. Amatucci and P. Stadelmann, *Microsc. Microanal.*, 2007, **13**, 87–95.
6 E. Negusse, Y. U. Idzerda and P. A. Suci, *J. Appl. Phys.*, 2004, **95**, 4506–4508.
7 B. Dieny, V. S. Speriosu, S. Metin, S. S. P. Parkin, B. A. Gurney, P. Baumgart and D. R. Wilhoit, *J. Appl. Phys.*, 1991, **69**, 4774–4779.
8 B. Dieny, V. S. Speriosu, S. S. P. Parkin, B. A. Gurney, D. R. Wilhoit and D. Mauri, *Phys. Rev. B: Condens. Matter Mater. Phys.*, 1991, **43**, 1297–1300.
9 M. Kiwi, *J. Magn. Magn. Mater.*, 2001, **234**, 584–595.
10 J. Nogués and I. K. Schuller, *J. Magn. Magn. Mater.*, 1999, **192**, 203–232.
11 J. W. Stout and L. M. Matarrese, *Rev. Mod. Phys.*, 1953, **25**, 338–343.
12 M. Griffel and J. W. Stout, *J. Am. Chem. Soc.*, 1950, **72**, 4351–4353.
13 R. A. Erickson, *Phys. Rev.*, 1953, **90**, 779–785.
14 L. Ming, M. Manghnani, T. Matsui and J. Jamieson, *Phys. Earth Planet. Inter.*, 1980, **23**, 276–285.
15 I. de, P. R. Moreira, R. Dovesi, C. Roetti, V. R. Saunders and R. Orlando, *Phys. Rev. B: Condens. Matter Mater. Phys.*, 2000, **62**, 7816–7823.
16 G. Valerio, M. Catti, R. Dovesi and R. Orlando, *Phys. Rev. B: Condens. Matter Mater. Phys.*, 1995, **52**, 2422–2427.
17 A. Riss, P. Blaha, K. Schwarz and J. Zemann, *Z. Kristallogr. Cryst. Mater.*, 2003, **218**, 585–589.
18 P. Novák, J. Kuneš, L. Chaput and W. E. Pickett, *Phys. Status Solidi B*, 2006, **243**, 563–572.
19 S. López-Moreno, A. H. Romero, J. Mejía-López, A. Muñoz and I. V. Roshchin, *Phys. Rev. B: Condens. Matter Mater. Phys.*, 2012, **85**, 134110.
20 F. Munoz, A. Romero, J. Mejía-López, I. V. Roshchin, R. González and M. Kiwi, *J. Magn. Magn. Mater.*, 2015, **393**, 226–232.
21 Y. Ma, G. K. Lockwood and S. H. Garofalini, *J. Phys. Chem. C*, 2011, **115**, 24198–24205.
22 H. Yamazaki and J. Satooka, *J. Phys.: Condens. Matter*, 2003, **15**, 1201.
23 P. Hohenberg and W. Kohn, *Phys. Rev.*, 1964, **136**, B864–B871.
24 W. Kohn and L. J. Sham, *Phys. Rev.*, 1965, **140**, A1133–A1138.
25 T. Liang, T.-R. Shan, Y.-T. Cheng, B. D. Devine, M. Noordhoek, Y. Li, Z. Lu, S. R. Phillpot and S. B. Sinnott, *Mater. Sci. Eng., R*, 2013, **74**, 255–279.
26 T. Liang, B. Devine, S. R. Phillpot and S. B. Sinnott, *J. Phys. Chem. A*, 2012, **116**, 7976–7991.
27 J. E. Mueller, A. C. T. van Duin and W. A. Goddard, *J. Phys. Chem. C*, 2010, **114**, 4939–4949.
28 M. J. Noordhoek, T. Liang, T.-W. Chiang, S. B. Sinnott and S. R. Phillpot, *J. Nucl. Mater.*, 2014, **452**, 285–295.
29 Y.-T. Cheng, T.-R. Shan, B. Devine, D. Lee, T. Liang, B. B. Hinojosa, S. R. Phillpot, A. Asthagiri and S. B. Sinnott, *Surf. Sci.*, 2012, **606**, 1280–1288.
30 K. Choudhary, T. Liang, A. Chernatynskiy, S. R. Phillpot and S. B. Sinnott, *J. Phys.: Condens. Matter*, 2015, **27**, 305004.
31 K. Choudhary, T. Liang, K. Mathew, B. Revard, A. Chernatynskiy, S. R. Phillpot, R. G. Hennig and S. B. Sinnott, *Comput. Mater. Sci.*, 2016, **113**, 80–87.
32 T. Liang, Y.-T. Cheng, X. Nie, W. Luo, A. Asthagiri, M. J. Janik, E. Andrews, J. Flake and S. B. Sinnott, *Catal. Commun.*, 2014, **52**, 84–87.
33 B. Devine, T.-R. Shan, Y.-T. Cheng, A. J. H. McGaughey, M. Lee, S. R. Phillpot and S. B. Sinnott, *Phys. Rev. B: Condens. Matter Mater. Phys.*, 2011, **84**, 125308.
34 T.-R. Shan, B. D. Devine, S. R. Phillpot and S. B. Sinnott, *Phys. Rev. B: Condens. Matter Mater. Phys.*, 2011, **83**, 115327.
35 T.-R. Shan, B. D. Devine, T. W. Kemper, S. B. Sinnott and S. R. Phillpot, *Phys. Rev. B: Condens. Matter Mater. Phys.*, 2010, **81**, 125328.
36 T.-R. Shan, B. D. Devine, J. M. Hawkins, A. Asthagiri, S. R. Phillpot and S. B. Sinnott, *Phys. Rev. B: Condens. Matter Mater. Phys.*, 2010, **82**, 235302.
37 Y.-T. Cheng, T.-R. Shan, T. Liang, R. K. Behera, S. R. Phillpot and S. B. Sinnott, *J. Phys.: Condens. Matter*, 2014, **26**, 315007.
38 A. Kumar, A. Chernatynskiy, T. Liang, K. Choudhary, M. J. Noordhoek, Y.-T. Cheng, S. R. Phillpot and S. B. Sinnott, *J. Phys.: Condens. Matter*, 2015, **27**, 336302.
39 T. Liang, M. Ashton, K. Choudhary, D. Zhang, A. F. Fonseca, B. C. Revard, R. G. Hennig, S. R. Phillpot and S. B. Sinnott, *J. Phys. Chem. C*, 2016, **120**, 12530–12538.
40 Y.-T. Cheng, T. Liang, J. A. Martinez, S. R. Phillpot and S. B. Sinnott, *J. Phys.: Condens. Matter*, 2014, **26**, 265004.
41 A. France-Lanord, P. Soukiassian, C. Glattli and E. Wimmer, *J. Chem. Phys.*, 2016, **144**, 104705.
42 S. Plimpton, *J. Comput. Phys.*, 1995, **117**, 1–19.
43 W. G. Hoover, *Phys. Rev. A: At., Mol., Opt. Phys.*, 1985, **31**, 1695–1697.
44 P. E. Blöchl, *Phys. Rev. B: Condens. Matter Mater. Phys.*, 1994, **50**, 17953–17979.
45 G. Kresse and D. Joubert, *Phys. Rev. B: Condens. Matter Mater. Phys.*, 1999, **59**, 1758–1775.
46 G. Kresse and J. Hafner, *Phys. Rev. B: Condens. Matter Mater. Phys.*, 1993, **47**, 558–561.
47 G. Kresse and J. Hafner, *Phys. Rev. B: Condens. Matter Mater. Phys.*, 1994, **49**, 14251–14269.
48 G. Kresse and J. Furthmüller, *Comput. Mater. Sci.*, 1996, **6**, 15–50.
49 G. Kresse and J. Furthmüller, *Phys. Rev. B: Condens. Matter Mater. Phys.*, 1996, **54**, 11169–11186.
50 J. P. Perdew, J. A. Chevary, S. H. Vosko, K. A. Jackson, M. R. Pederson, D. J. Singh and C. Fiolhais, *Phys. Rev. B: Condens. Matter Mater. Phys.*, 1992, **46**, 6671–6687.

51 J. P. Perdew, K. Burke and M. Ernzerhof, *Phys. Rev. Lett.*, 1996, **77**, 3865–3868.
52 S. L. Dudarev, G. A. Botton, S. Y. Savrasov, C. J. Humphreys and A. P. Sutton, *Phys. Rev. B: Condens. Matter Mater. Phys.*, 1998, **57**, 1505–1509.
53 J. Sun, A. Ruzsinszky and J. P. Perdew, *Phys. Rev. Lett.*, 2015, **115**, 036402.
54 J. Sun, R. C. Remsing, Y. Zhang, Z. Sun, A. Ruzsinszky, H. Peng, Z. Yang, A. Paul, U. Waghmare and X. Wu, *et al.*, *Nat. Chem.*, 2016, **8**, 831.
55 J. Tersoff, *Phys. Rev. B: Condens. Matter Mater. Phys.*, 1988, **37**, 6991–7000.
56 A. Yasukawa, *JSME Int. J., Ser. A*, 1996, **39**, 313–320.
57 F. H. Streitz and J. W. Mintmire, *Phys. Rev. B: Condens. Matter Mater. Phys.*, 1994, **50**, 11996–12003.
58 J. Gale and A. Rohl, *Mol. Simul.*, 2003, **29**, 291–341.
59 J. A. Rayne and B. S. Chandrasekhar, *Phys. Rev.*, 1961, **122**, 1714–1716.
60 N. Zotov and A. Ludwig, *Intermetallics*, 2008, **16**, 113–118.
61 W. H. Baur, *Acta Crystallogr.*, 1958, **11**, 488–490.
62 A. Y. Wu, R. J. Sladek and R. S. Feigelson, *Phys. Rev. B: Condens. Matter Mater. Phys.*, 1982, **26**, 1507–1511.
63 H. J. Monkhorst and J. D. Pack, *Phys. Rev. B: Solid State*, 1976, **13**, 5188–5192.
64 J. A. Niesse and H. R. Mayne, *J. Chem. Phys.*, 1996, **105**, 4700–4706.
65 A. Romero and J. Mejía-López, *Phys. B*, 2006, **384**, 244–248.
66 M. Winter, The Periodic Table by WebElements, The University of Sheffield and WebElements Ltd, UK, https://www.webelements.com/.
67 E. Giner, A. Scemama and M. Caffarel, *J. Chem. Phys.*, 2015, **142**, 044115.
68 A. Kleibert, W. Rosellen, M. Getzlaff and J. Bansmann, *Beilstein J. Nanotechnol.*, 2011, **2**, 47–56.
69 Q.-M. Ma, Z. Xie, J. Wang, Y. Liu and Y.-C. Li, *Solid State Commun.*, 2007, **142**, 114–119.
70 O. Diéguez, M. M. G. Alemany, C. Rey, P. Ordejón and L. J. Gallego, *Phys. Rev. B: Condens. Matter Mater. Phys.*, 2001, **63**, 205407.
71 G. von Eynatten and H. E. Bömmel, *Appl. Phys.*, 1977, **14**, 415–421.
72 M. Kiwi, J. Mejía-López, R. D. Portugal and R. Ramírez, *EPL*, 1999, **48**, 573.
73 M. Kiwi, J. Mejía-López, R. D. Portugal and R. Ramírez, *Appl. Phys. Lett.*, 1999, **75**, 3995–3997.
74 M. Kiwi, J. Mejía-López, R. D. Portugal and R. Ramírez, *Solid State Commun.*, 2000, **116**, 315–319.
75 J. Mejía-López, P. Soto and D. Altbir, *Phys. Rev. B: Condens. Matter Mater. Phys.*, 2005, **71**, 104422.
76 COMB parametrized potential for Fe and FeF2, http://neel.fis.puc.cl/cncm/COMB_potential_Fe–F, accessed: 2019-07-24.
77 A. K. Rappe and W. A. Goddard, *J. Phys. Chem.*, 1991, **95**, 3358–3363.
78 X. W. Zhou, H. N. G. Wadley, J.-S. Filhol and M. N. Neurock, *Phys. Rev. B: Condens. Matter Mater. Phys.*, 2004, **69**, 035402.
79 D. Wolf, P. Keblinski, S. R. Phillpot and J. Eggebrecht, *J. Chem. Phys.*, 1999, **110**, 8254–8282.
80 L. Jensen, P.-O. Åstrand, A. Osted, J. Kongsted and K. V. Mikkelsen, *J. Chem. Phys.*, 2002, **116**, 4001–4010.
81 H. Wang and W. Yang, *J. Chem. Phys.*, 2016, **144**, 224107.
82 H. Toufar, K. Nulens, G. O. A. Janssens, W. J. Mortier, R. A. Schoonheydt, F. De Proft and P. Geerlings, *J. Phys. Chem.*, 1996, **100**, 15383–15387.
83 D. W. Brenner, O. A. Shenderova, J. A. Harrison, S. J. Stuart, B. Ni and S. B. Sinnott, *J. Phys.: Condens. Matter*, 2002, **14**, 783.
84 B. J. Thijsse, *Nucl. Instrum. Methods Phys. Res., Sect. B*, 2005, **228**, 198–211.

